30th AIAA Applied Aerodynamics Conference
25 - 28 June 2012, New Orleans, Louisiana

AIAA 2012-2781

CFD Analysis of Multielement Airfoils for Wind Turbines

Shreyas Narsipur,* Brent W. Pomeroy,† and Michael S. Selig‡
University of Illinois at Urbana-Champaign, Urbana, IL 61801, USA

Multielement airfoil configurations have shown promise in improving the aerodynamic characteristics of the inboard section of megawatt-scale wind turbine blades by increasing the lift-to-drag ratios, lift coefficients, and structural efficiency. Steady-state, two-dimensional CFD calculations were carried out for a closely-coupled multielement airfoil system with one main element and two flaps at a Reynolds number of 1,000,000. Five configurations of the multielement airfoil system were simulated with varying flap deflection, gap, and overhang. Simulations were performed with ANSYS FLUENT, which is a hybrid-grid Navier-Stokes solver. Computational results were obtained using the four-equation Langtry-Menter Shear Stress Transport (SST) Transition turbulence model. Grid convergence studies were carried out by examining three grids with progressively higher grid resolutions and quantifying their effects on lift and drag coefficients. Computed solutions were obtained for angles of attack ranging from 9 to 20 deg. Lift and drag coefficients were computed to understand the effect of gap, overhang, and flap deflection on the multielement airfoil system performance. Wake bursting, a multielement airfoil phenomenon, was observed by visualizing off-the-surface flow downstream of the airfoil.

Nomenclature

A = mesh area
c = airfoil chord
C_d = 2D drag coefficient
C_l = 2D lift coefficient
C_p = pressure coefficient
c_{sys} = system chord length
e_{app} = approximate error
e_∞ = extrapolated relative error
h = average mesh size
N = total number of cells
o = order of solution
P_0 = stagnation pressure
P_{atm} = atmospheric pressure
q = total number of grids
r = grid refinement factor
Re = Reynolds number
t/c = thickness-to-chord ratio
U = local velocity
U_∞ = freestream velocity
x/c = normalized chordwise location
y^+ = non-dimensional distance from airfoil surface
z_{gn} = flap gap of element n relative to element $n-1$
z_{on} = flap overhang of element n relative to element $n-1$

*Graduate Student, Department of Aerospace Engineering, and AIAA Student Member
†Graduate Student, Department of Aerospace Engineering, and AIAA Student Member
‡Associate Professor, Department of Aerospace Engineering, and AIAA Senior Member

α = angle of attack
δ_n = absolute deflection angle of element n
$\delta_{r,n}$ = relative deflection angle of element n
φ = variable of simulation

I. Introduction

Since the last decade, the need to extract wind energy has become important because of the rise in energy demands and interests in renewable energy. There have been major advancements in the designs of the modern wind turbines to meet the growing energy needs. Wind energy as a power source is attractive as an alternative to fossil fuels because it is abundant, renewable, widely distributed, clean, and produces no greenhouse gas emissions.

With increasing energy requirements, the need to design larger and more efficient wind turbines has become the primary focus in wind turbine research. However, increasing the swept area of the rotor blades to generate more power leads to structural complications as the weight of the wind turbine blades increases with the volume of the blade. This trend is known as the square-cubed law. The competing structural and aerodynamic requirements causes an overall loss in the aerodynamic efficiency of the wind turbine.[1]

Inboard sections of modern megawatt-scale wind turbines consist of thick airfoils to maintain the structural integrity of the blade. However, thick airfoils are prone to having sub-optimal aerodynamic performance due to sharp stall characteristics, increased pressure drag, and aerodynamic noise owing to trailing-edge vortex shedding.

Multielement airfoil configurations placed in the root section of wind turbine blades have been shown to improve the aerodynamic characteristics of the blades which can reflect in an overall performance improvement of the wind turbine.[2] Unlike high-lift devices such as flaps and slats on aircraft, which are stored within the main element during cruise, multielement airfoils for wind turbines are designed based on tip speed ratio for a single angle of attack and do not need to be moved during operation. The fixed positions of the elements makes them a simple and feasible option for improving blade performance. The aim of this research was to computationally analyze the aerodynamics of a multielement airfoil system for wind turbines.

The multielement airfoil system chosen for this study was a closely-coupled three-element system consisting of one main element and two flap elements as shown in Fig. 1. The airfoil system, designed by Ragheb and Selig,[2] has a system chord length (c_{sys}) of unity and aims to replace DU 00-W-401–like airfoils at the root section of wind turbine blades. Computations were performed for various configurations of the closely-coupled system where each configuration represents a different flap deflection, gap, and overhang. Numerical simulations were focused on visualizing and analyzing lift, drag, pressure, and downstream wake characteristics of the multielement airfoil system in steady flow. Five configurations were chosen, and numerical simulations were performed using the hybrid grid Reynolds Averaged Navier-Stokes solver, ANSYS® FLUENT™.

Studies by Smith[3] in 1975 show that multielement airfoil systems have complex flow characteristics as numerous effects govern the flow around these systems. It became necessary to generate the computational grids and choose a computational turbulence model that could capture the complex flow phenomena around the multielement airfoil.

Initial studies were primarily focused on choosing the best turbulence model for the numerical simulations of the multielement airfoil system. The turbulence model is critical to the computational solution and care must be taken to choose a model that can accurately compute and resolve the complex flow around the multielement airfoil system. Most of the turbulence models available within ANSYS FLUENT consider the flow to be completely turbulent and do not model flow transition on the airfoil, thereby overpredicting C_d. Based on the Langtry-Menter turbulence model formulation and validation,[4] the SST Transition turbulence model was selected for validation. Turbulence model validation was performed by computationally analyzing the NLR 7301 airfoil section with a trailing-edge flap and comparing the lift, drag, and pressure coefficient results with experimental data.[5,6] Based on the validation study, the SST Transition turbulence model was chosen for all computations as it had the capability of resolving the complex aerodynamic flows associated with multielement airfoil systems.

Grid refinement and validation studies were performed to choose the appropriate grid size as computational grids play a vital role in accurately resolving the complex flow fields. For the grid validation studies,

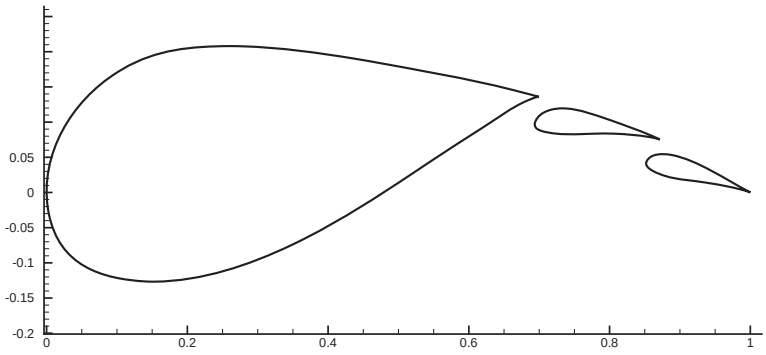

Figure 1. Closely coupled multielement airfoil system.

three grids with increasing grid resolution were generated and solved for the baseline configuration of the closely-coupled multielement airfoil system. Based on the results obtained from the grid validation studies, default grid parameters were set up for the remainder of the multielement airfoil configurations. Computations for each multielement airfoil configuration were performed at a freestream Reynolds number of 1×10^6 for nine angles of attack. The following sections discuss the turbulence model and grid validation studies, approach used for solving the computations, and the results obtained from the closely-coupled multielement airfoil system simulations.

II. Turbulence Model Validation

Validation of a turbulence model is essential in determining if the model is applicable to the current computational problem. For the current research, the four-equation Langtry-Menter SST Transition turbulence model was chosen for the validation studies. The SST Transition model is a four-equation model with the SST k-ω transport equations in terms of moumentum-thickness Reynolds number, which help in predicting transition over geometries accurately and resolves complex aerodynamic flows over multiple airfoils.[4]

The SST Transition turbulence model was validated by simulating the NLR 7301 supercritical airfoil/flap configuration and comparing the lift and drag curves against experimental data collected in the low speed wind tunnel at the National Research Labs, Netherlands.[5,6] The experimental data also included pressure distributions at angles of attack of 6 and 13.1 deg. The two-element system consisted of the NLR 7301 airfoil section and a flap element of 32% chord at a deflection angle of 20 deg, a gap of 2.6% chord, and an overhang of 5.3% chord, as shown in Fig. 2. The simulations were performed at freestream conditions corresponding to those of the experiments. The following sections give details about the grid generated for the NLR 7301 airfoil/flap configuration and then compare the simulation results with experimental data.

A. Computational Grid

Computational solutions are sensitive to the discretization of the computational domain. For the present 2D computations, zonal hybrid grids, as shown in Fig. 3, were generated with structured cells consisting of quadrilateral elements in the boundary layer region of the airfoil and unstructured cells consisting of triangular elements for the rest of the domain. Computational domain area, wall y^+, grid growth rate, and number of viscous boundary layers were the focal grid parameters while generating the grids.

The computational domain is the geometrical region which bounds the numerical simulation. The distance of the far-field region from the surface of the airfoil must be such that the effects of the flow at the far-field region do not have an impact on the near-field solution. The computational domain area is determined by the far-field distance given in terms of the chord length of the airfoil under consideration. Computational domain area for the present grids were defined by placing the far-field boundaries at 15 times the system chord length (c_{sys}). This distance translates to a computational domain area of $30c_{sys} \times 30c_{sys}$.

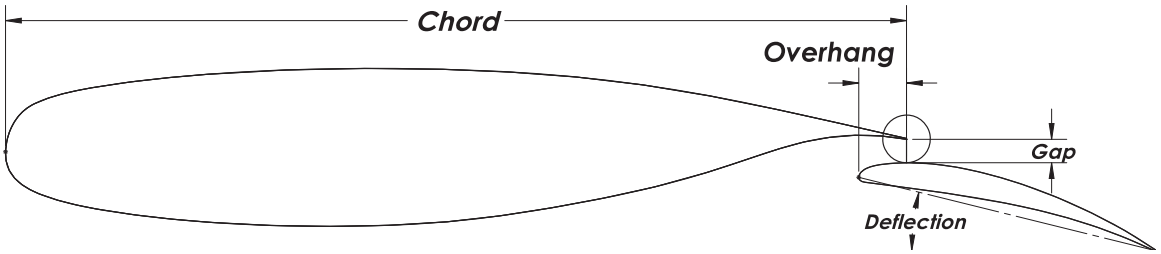

Figure 2. NLR 7301 multielement airfoil configuration.[6]

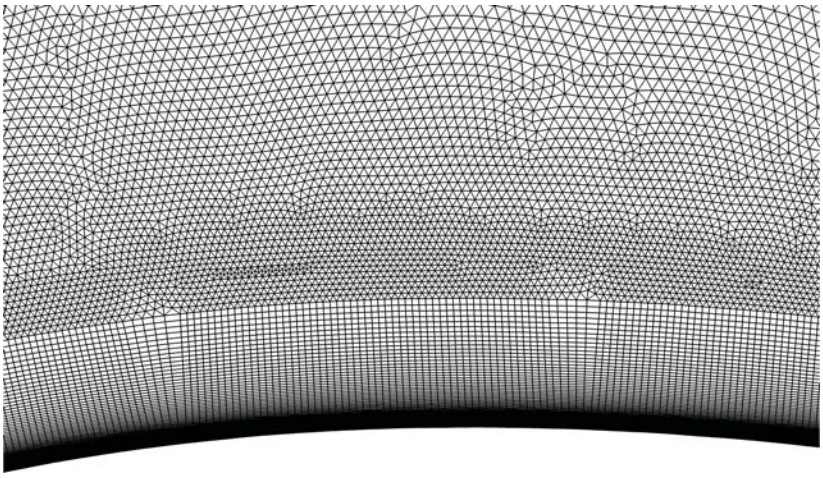

Figure 3. Zonal hybrid grid eminating from the airfoil surface (3% of chord is shown).

Wall y^+ is a non-dimensional distance perpendicular to the airfoil surface and is proportional to the ratio of the friction velocity at the wall and the kinematic viscosity of the fluid. The wall y^+ to be employed is determined by the turbulence model being used to solve the flow in the computational domain. An important requirement in the application of wall functions in CFD is that the cells adjacent to the wall have a height (usually expressed in y^+ units) that is compatible with the wall functions. For the SST Transition model to accurately resolve the boundary layer flow, y^+ was set to be less than unity throughout the surface of each element of the multielement airfoil system.

Grid growth rate is defined as the rate at which grid cell size increases as the grid layers advance from the airfoil surface to the boundaries defined by the computational domain. With increasing order of grid resolution, the value of the grid growth rate decreases.

The number of viscous layers in the boundary layer determines the computational resolution of the flow gradients near the surface of the airfoil. Proper resolution of the flow gradients is critical in obtaining accurate results. For the present grids, the number of viscous layers increased with increasing level of grid resolution.

Values for the grid parameters were decided based on the multielement airfoil system chord length, turbulence model, and freestream Reynolds number. The final grid for the NLR 7301 supercritical airfoil/flap configuration, as shown in Fig. 4, consisted of 8,267 nodes on the surface of the main element and 1,612 nodes on the surface of the flap element. The number of structured cells in the boundary layer was 1,333,390, and the total number of cells in the computational domain was 2,077,261. Larger cell concentration was used near the leading and trailing edges of each element and between the gaps of the elements. The first node adjacent to the wall of the main element and the flap element was at a distance of $y = 5.70\times10^{-6}$ and $y = 1.90\times10^{-6}$ respectively to obtain a $y^+ = 1$ for a freestream chord Reynolds number of 2.51×10^6 corresponding to Refs. 5, 6. The computational domain area was 30×30.

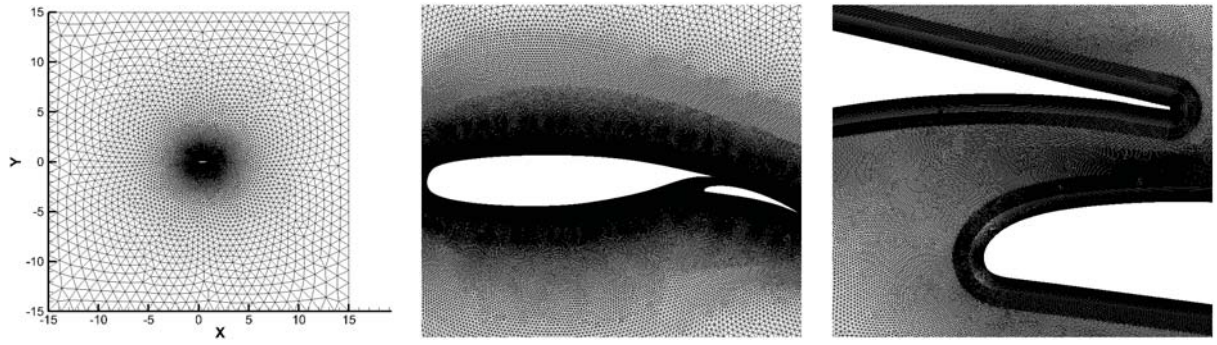

(a) Computational domain (b) Grids around the airfoil (c) Grids between the gaps

Figure 4. Grids for the NLR 7301 airfoil/flap configuration.

B. Solution Development

All solutions in this study were computed using the Reynolds Averaged Navier-Stokes solution scheme. Numerical analysis was done using the pressure-based solver by applying the transport equations at the nodes of the grid elements. The Langtry-Menter four-equation SST Transition model was used for all computations. The simulations for the NLR 7301 airfoil/flap configuration were made at $Re = 2.51\times10^6$ (based on c_{sys}) and a freestream temperature of 300 K (80.33 °F). The flow initialization for the multielement airfoil configuration took 50 hours and 55,000 iterations before solution convergence. The computations were performed on a desktop system with an Intel® Core™ i7 quad core processor with 9 GB of RAM. The grid was split into four zones, each of which were computed by a single processor.

C. Results and Comparison

1. Lift and Drag Characteristics

Comparison of computational C_l and C_d with experimental data at various angles of attack is shown in Fig. 5. It is observed from Fig. 5 that computed C_l and C_d are in good agreement with the experimental data. The SST Transition turbulence model underpredicts C_l by ≈3% constantly and overpredicts C_d by ≈4% for all angles of attack.

It can also be observed from Fig. 5 that the trends of the computed lift curve and drag polar are similar to that of the experimental data. The low error in the prediction of C_l and C_d by the SST Transition model can be attributed to the fact that flow transition was being modeled and that the laminar and turbulent boundary layers were well resolved.

2. Pressure Coefficient Distribution

Figure 6 shows the computed C_p distribution over the surface of the airfoil compared with the experimental data for angles of attack of 6 and 13.1 deg respectively. It can be observed from Fig. 6 that the SST Transition model predicts the C_p distribution with good accuracy.

Based on the accuracy of lift, drag, and pressure coefficient prediction by the SST Transition model, the turbulence model validation study was concluded, and the SST Transition turbulence model was chosen for all further simulations of the closely-coupled multielement airfoil system.

III. Closely-Coupled Multielement Airfoil System

The closely coupled multielement airfoil system, shown in Fig. 7, was designed as a replacement airfoil system for an existing single-element wind turbine airfoil.[2] A system chord length of unity was defined for all configurations. The leading edge of the multielement system was not necessarily the leading edge of the main element. Flap deflections were defined, and the trailing edge of the final flap was set on the system chord line of $y = 0$, as shown in Fig. 7, and defined as the trailing edge of the system (TE_{sys}). The leading

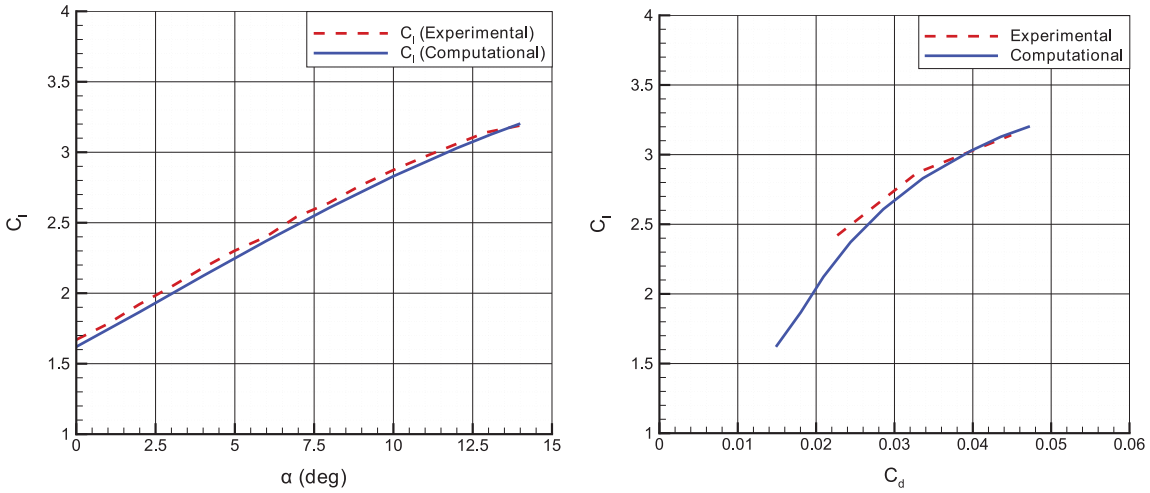

(a) C_l vs. α (b) C_l vs. C_d

Figure 5. Comparison plots of lift and drag coefficient for NLR 7301 multielement airfoil configuration.[5,6]

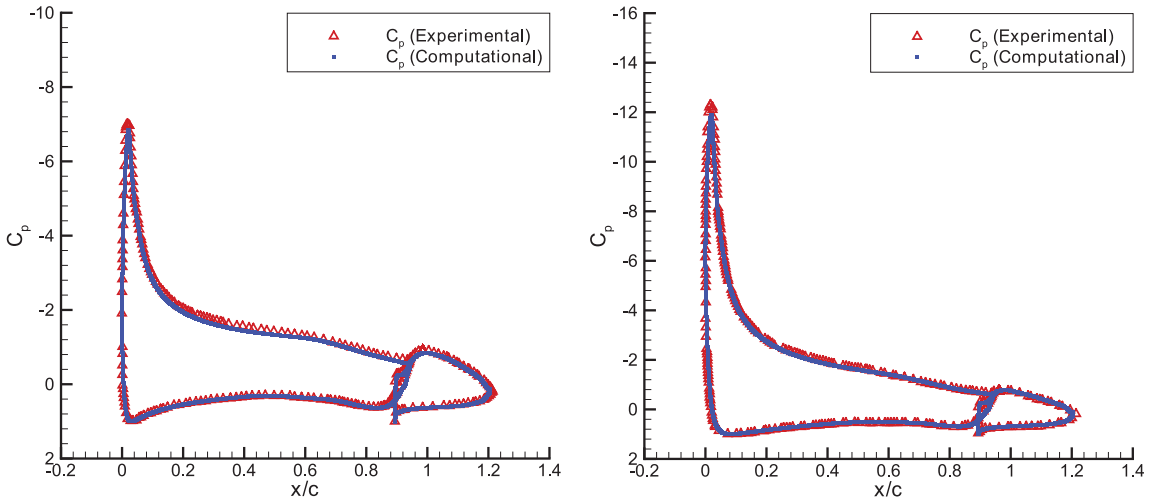

(a) C_p distribution at $\alpha = 6$ deg (b) C_p distribution at $\alpha = 13.1$ deg

Figure 6. Comparison plots of pressure coefficient for NLR 7301 multielement airfoil configuration.[6]

edge of the system (LE_{sys}) was defined as the point furthest away from the trailing edge of the system and was set at the origin. The angle of attack was defined as the angle between the freestream velocity and the system chord line. The airfoil system can be described in terms of relative coordinates with the position of each element defined by the position of the leading edge and flap angle (three degrees of freedom).

The aerodynamic performance of multielement airfoil systems is highly dependent on deflection angles, overhang distance, and gap sizes between the elements.[7,8] The relative coordinate system, shown below in Fig. 7, was used to define the system by parameters which govern the flow. The deflection angle of the main element (δ_1) was taken as zero. A positive deflection angle corresponded to a downward flap deflection. The location of the flaps was constrained by overhang distance and gap size. The gap size between elements (Gap_n) was defined as the distance from the trailing edge of element n to the closest point on element $n+1$. Overhang distance ($Overhang_n$) between elements n and $n+1$ was defined as the distance from the leading edge of element $n+1$ to the trailing edge of n projected along the chord line of element n, as shown in the lower portion of Fig. 7. A positive overhang indicates that the leading edge of the flap is ahead of the trailing edge of the previous element. Relative deflection angles ($\delta_{r,n}$) were defined as the angle between the chord line of element $n+1$ and the chord line of element n.

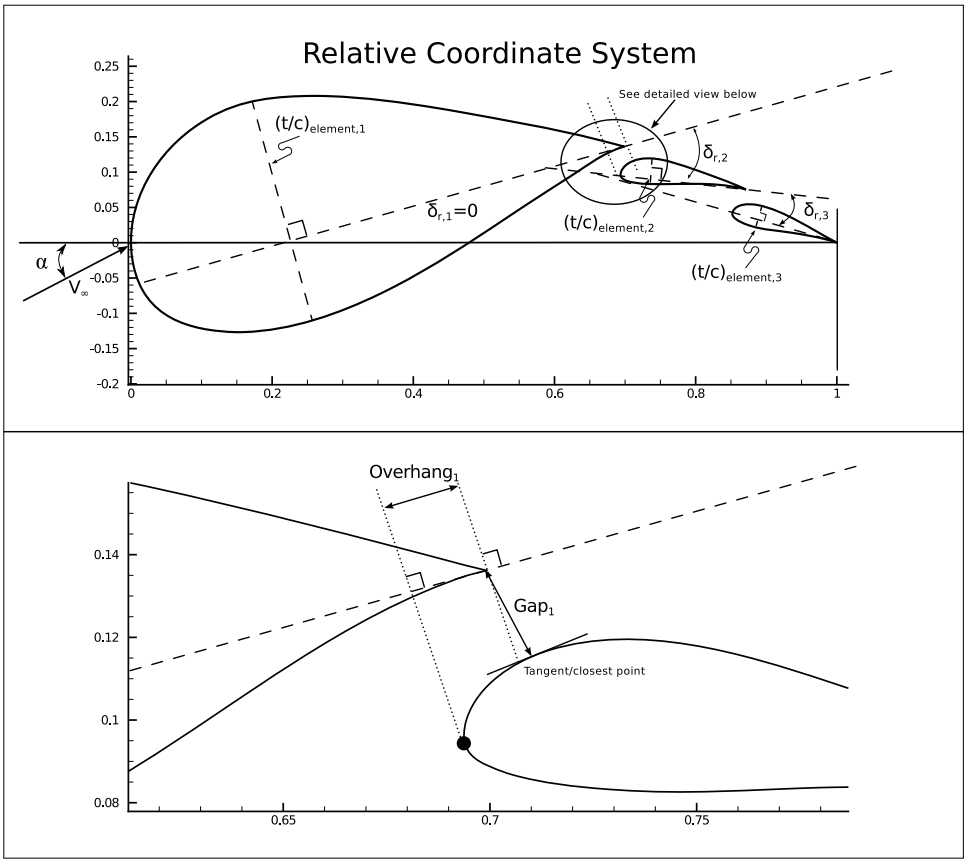

Figure 7. Relative coordinates for closely-coupled multielement airfoil system.

IV. Computational Approach

A systematic grid validation study was conducted for a single configuration of the multielement airfoil system. Convergence criteria adopted for grid validation studies are described, and the representative plots are shown.

A. Grid Validation

Numerical solutions are highly sensitive to the discretization of the computational domain. Based on the grid parameters set during the validation process, three grids (coarse, medium, and fine), as shown in Fig. 8, were generated for the baseline configuration of the closely-coupled system, henceforth referred to as CC-1. Grid growth rate and number of viscous boundary layers were the grid parameters varied for the three grids. Details of the three grids are given in Table 1. Steady-state simulations using the SST Transition turbulence model were performed for the three grids for a $Re = 1 \times 10^6$ at an angle of attack of 9.081 deg with the same boundary conditions.

Table 1. Grid Statistics for the Grid Validation of CC-1

Grid	Number of cells in boundary layer	Total number of cells
Coarse	872,895	1,104,547
Medium	1,022,764	1,456,130
Fine	1,588,164	2,369,176

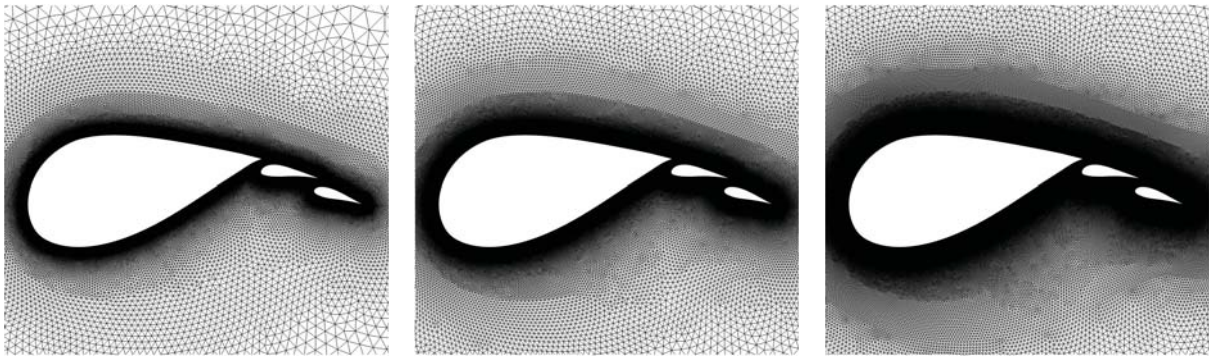

(a) coarse (b) medium (c) fine

Figure 8. Grids for grid validation of CC-1.

1. *Grid Convergence Index*

Grid Convergence Index (GCI) is a method to calculate the order of convergence. GCI provides an estimate of the uncertainty in the converged solution and gives an indication of how much the solution will change with further grid refinement. The computed solution should approach an asymptotic value (i.e., the true numerical solution) as the grid is refined and the resolution is improved. The procedure presented by Celik, et al.[9] to determine GCI was used for this analysis. First the average grid size for the complete computational domain was determined from the equation

$$h = \left(\frac{1}{N} \sum_{i=1}^{N} \Delta A_i \right)^{\frac{1}{2}} \tag{1}$$

where N is the total number of cells in the domain and ΔA_i is the area of the i^{th} cell. Next, the grid refinement factor was obtained using the equation

$$r_{ij} = \frac{h_i}{h_j} \tag{2}$$

where the coarser grid is represented by i and the finer grid is represented by j. The apparent order, o, of the transport equations used in the computations was calculated using the expression

$$o = \frac{1}{ln\ r_{(q-1)q}} ln \left[\left(\frac{\varphi_{(q-1)} - \varphi_{(q-2)}}{\varphi_q - \varphi_{(q-1)}} \right) \right] \tag{3}$$

where φ is a variable of the simulation (C_d for the current grid validation studies). The total number of grids used for the validation process arranged in increasing order of fineness is represented by q. The extrapolated solution for an infinitely large mesh was calculated from the expression

$$\varphi_\infty = \frac{r^{(q-1)q} \varphi_q - \varphi_{(q-1)}}{r^{(q-1)q} - 1} \tag{4}$$

The approximation of the total computation error was obtained using

$$e_{app} = \left| \frac{\varphi_q - \varphi_{(q-1)}}{\varphi_q} \right| \tag{5}$$

Similarly, the extrapolated relative error was calculated using

$$e_\infty = \left| \frac{\varphi_q - \varphi_{(q-1)}}{r^{(q-1)q} \varphi_q - \varphi_{(q-1)}} \right| \tag{6}$$

Finally, the GCI was determined from the following expression

$$GCI = \frac{1.25 e_{app}}{r^o_{(q-1)q} - 1} \tag{7}$$

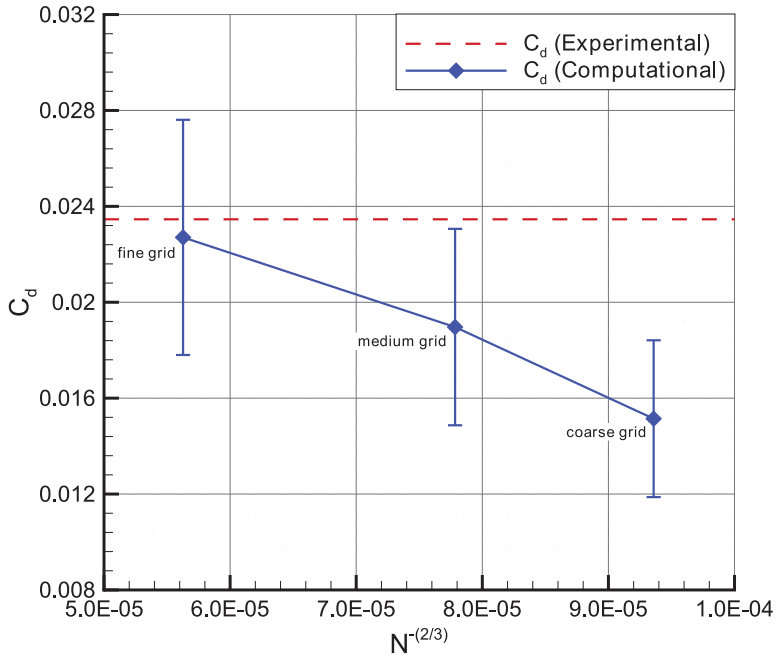

Figure 9. Grid convergence of C_d from the SST Transition turbulence model.

For the present grid convergence study, the true solution was taken as the negative bound of the extrapolated solution, i.e.

$$True\ Solution = \varphi_\infty - e_\infty \varphi_\infty \tag{8}$$

The computational C_d data obtained was used to calculate the GCI, true solution, and the resulting bounds of C_d for each grid. A summary of the results is shown in Table 2 and plotted in Fig. 9. It can be seen from Fig. 9 that the finest grid is closest to the true solution of C_d. Also the true solution lies within the uncertainty bounds of the computed solution using the finest grid. Hence the grid parameters associated with the fine grid were set as default, and similar grids were generated for the remaining configurations of the closely-coupled multielement airfoil system.

2. Representative Residuals

For every computational simulation, the flow and turbulence model residuals were monitored. The solution was considered to have converged if the representative residuals were of the order of 10^{-6} units. The average flow and turbulence model residuals and C_l and C_d for the last 4,000 iterations of CC-1 simulations were plotted for the fine grid and are shown in Fig. 10(a–b), respectively. From Fig. 10(b), it can be observed that the deviation in the values of C_l and C_d is small over the last 4,000 iterations suggesting that the solution has converged.

Table 2. Summary of the Grid Validation Process

Grid	Total number of cells (N)	$N^{-(2/3)}$	C_d Computational	C_d True Solution	GCI	Positive bound	Negative bound
Coarse	1,104,547	9.35×10^{-5}	0.015143	0.023460	0.216	0.018413	0.011872
Medium	1,456,130	7.78×10^{-5}	0.018965	0.023460	0.216	0.023061	0.014868
Fine	2,369,176	5.62×10^{-5}	0.022706	0.023460	0.216	0.027610	0.017801

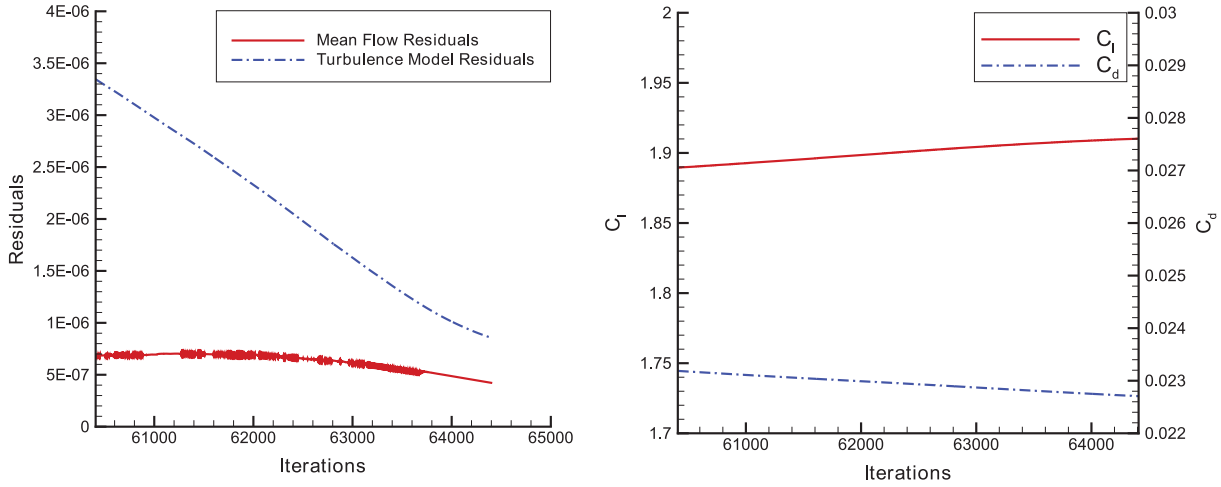

(a) Average flow and turbulence model residuals.

(b) Variation of C_l and C_d with iterations

Figure 10. Representative residuals of the fine grid.

B. Solution Development

On completion of the grid validation process, the grid parameters were fixed for all multielement airfoil configurations. The grids used for computing the solutions for the closely-coupled configurations are shown in Fig. 11. Table 3 summarizes the boundary layer grids on each element of the multielement airfoil system. The total number of structured cells in the boundary layer was 1,588,164, and the total number of cells in the computational domain was 2,369,176. Larger cell concentration was used near the leading and trailing edges of each element, between the gaps of the elements, and at the wake of the multielement airfoil system. All solutions were computed using the pressure-based solver by applying the Langtry-Menter four-equation SST Transition model transport equations at the nodes of the grid elements. The flow initialization for each closely-coupled configuration took 70 hours and 65,000 iterations before solution convergence. The remaining angles of attack for a configuration were computed in 20 hours and 10,000 iterations as they were initialized using the converged solution of the previous angle of attack.

V. Results and Discussion

All computations for the closely-coupled system were made at $Re = 1{\times}10^6$ (based on c_{sys}) and a freestream temperature of 300 K (80.33 °F). Five configurations with varying gap, overhang, and flap deflection angles, as summarized in Table 4, were chosen. Solutions have been computed at nine different angles of attack for each configuration, with all angles of attack being restricted to the linear region of the lift curve (prior to stall).

On completion of the simulations, lift curve and drag polar for each configuration was generated, co-plotted, and analyzed. The pressure coefficient distributions at selected angles of attack for the baseline configuration were studied and compared. The U/U_∞ contour plots were studied in detail to visualize and analyze the complex flow fields in the wake region of the closely-coupled multielement airfoil system.

Table 3. Summary of Boundary Layer Grids on Individual Elements of the Closely-Coupled System

Element	Number of surface nodes	Location of first node above airfoil surface, y (for Re=$1{\times}10^6$)	Number of viscous boundary layers
Main	8,267	$1.65{\times}10^{-5}$	51
Flap 1	1,891	$4.10{\times}10^{-6}$	79
Flap 2	1,612	$3.50{\times}10^{-6}$	81

(a) Computational domain (b) Grids around the airfoil (c) Grids between the gaps

Figure 11. Grids for the closely-coupled configurations.

A. Lift and Drag Characteristics

Plots of computational lift and drag polars at $Re = 1{\times}10^6$ for the five closely coupled configurations were co-plotted and are shown in Figs. 12 and 13. As shown in Table 4, configurations CC-1, CC-11, and CC-15 have the same flap gaps and overhangs while the flap deflections are changed. For configurations CC-15, CC-40, and CC-53, the flap deflections are held constant while the gaps and overhangs are varied. Figure 12 compares the C_l and C_d data for the cases with varying flap deflections while Fig. 13 shows similar plots for varying gap and overhang.

In the case of constant flap gaps and overhangs and varying flap deflections, it can be observed from Fig. 12(a) that as the flap deflections are increased from CC-1 to CC-15, the lift increases significantly. The increase in lift can be attributed to the fact that increasing flap deflection leads to higher camber on the multielement system causing higher flow curvature, thereby increasing lift. The results observed in Fig. 12(a) agree with the studies on a two-element slotted flap multielement airfoil system carried out by Biber, et al.[10] who concluded that an increase in flap deflection angle increases C_l at a given α. The results shown in Fig. 12(a) also agree well with the studies carried out by Cerra and Katz[7] on the effect of flap deflection on C_l of a thick airfoil system as shown in Fig. 14. It is also interesting to note from Fig. 12(a) that an increase in δ_3 along with a slight decrease in δ_2 starting from the baseline configuration CC-1 to CC-11 does not increase C_l significantly. It can be concluded that C_l is more sensitive to the deflection of the first flap (δ_2) as compared with the deflection of the second flap (δ_3). There is no significant effect of varying flap deflections on C_d for the closely-coupled multielement airfoil system.

Cross comparison of C_l for constant flap deflections and varying gaps and overhangs, as shown in Fig. 13(a), shows that increasing gap and decreasing overhang does not have a significant effect on the lift of the closely-coupled multielement airfoil system. However, decreasing both gap and overhang causes a decrease in the lift curve slope. In general, a smaller gap accelerates the flow more rapidly than a larger gap. Spaid[11] observed that confluent boundary layers and complex wake interactions due to gaps being too small reduce the multielement airfoil system performance. The effect of the gap size as observed by Ashby[8] is presented in Fig. 15.

Table 4. Details of Closely-Coupled Configurations Simulated

Configuration	Gap_2 ($\%c_{sys}$)	$Overhang_2$ ($\%c_{sys}$)	$\delta_{r,2}$ (deg)	Gap_3 ($\%c_{sys}$)	$Overhang_3$ ($\%c_{sys}$)	$\delta_{r,3}$ (deg)
CC-1 (baseline)	0.022828	0.014340	21.40	0.020112	0.014740	9.03
CC-11	0.022828	0.014340	21.00	0.020112	0.014740	11.00
CC-15	0.022828	0.014340	23.00	0.020112	0.014740	13.00
CC-40	0.027828	0.006840	23.00	0.027828	0.006840	13.00
CC-53	0.015000	0.010000	23.00	0.015000	0.010000	13.00

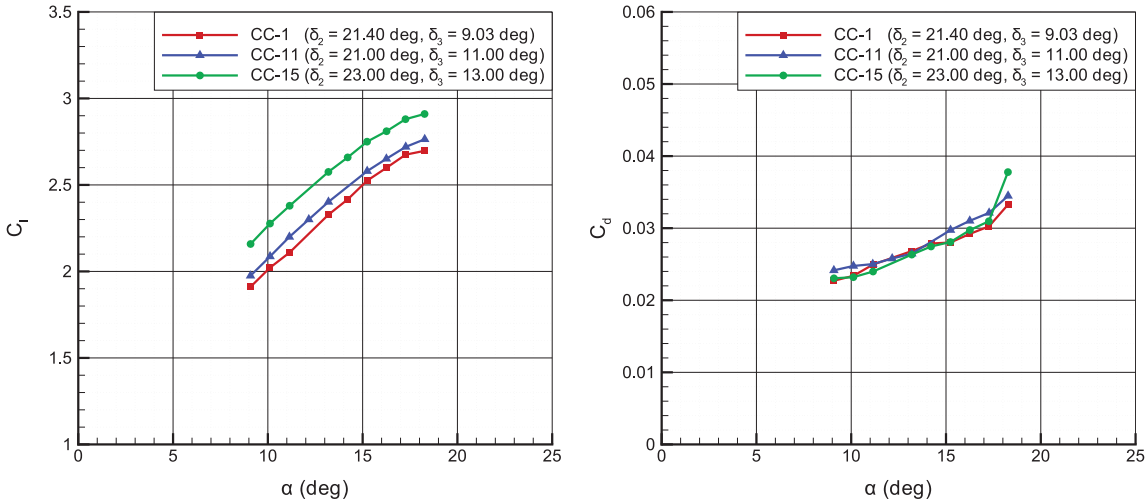

(a) C_l vs. α (b) C_d vs. α

Figure 12. Cross comparison plots for constant flap gaps and overhangs at $Re = 1\times10^6$.

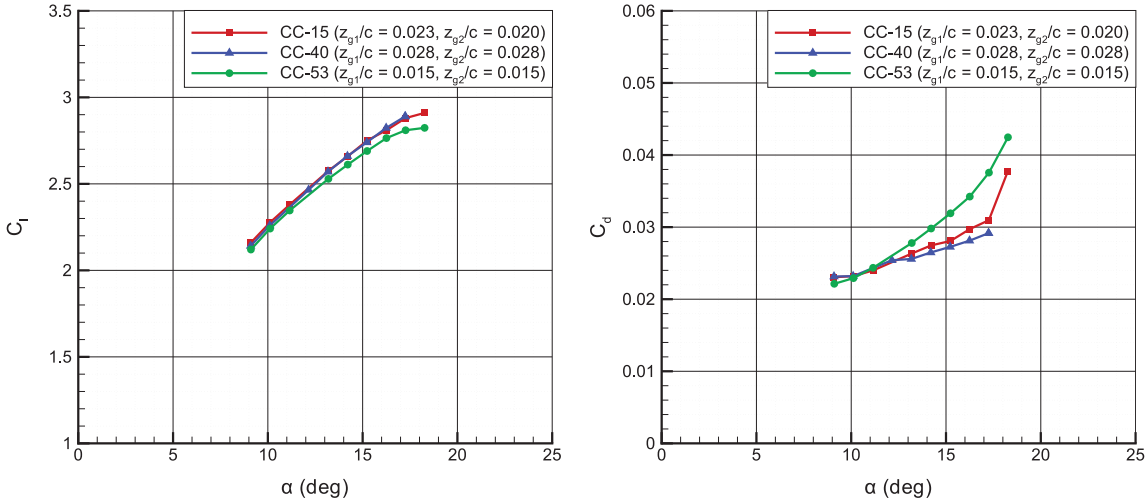

(a) C_l vs. α (b) C_d vs. α

Figure 13. Cross comparison plots for constant flap deflections at $Re = 1\times10^6$.

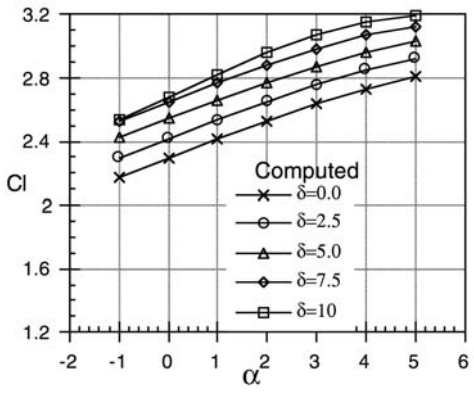

Figure 14. Computational results indicating effect of flap deflection on C_l ($Re = 1\times10^6$) (taken from Ref. 7).

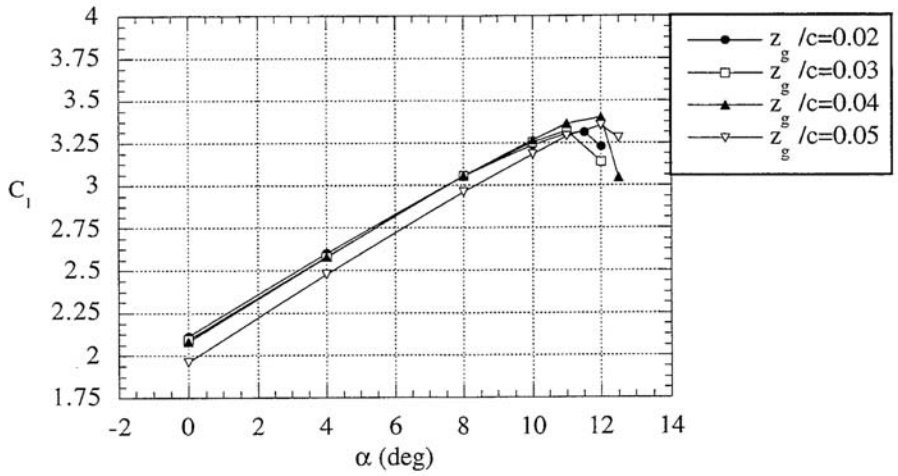

Figure 15. Experimental results indicating effect of gap size on C_l at $Re = 3.5\times10^6$ (taken from Ref. 8).

The trends observed in the lift curves in Fig. 13(a) for the closely-coupled multielement airfoil system are similar to those observed by Ashby (Fig. 15).[8] Figure 13(b) shows that C_d of the closely-coupled system is highly dependent on the flap gap and overhang. The sensitivity of C_d to variations in flap gap and overhang is due to wake effects downstream of the airfoil.

B. Coefficient of Pressure Distribution

Figure 16 shows the pressure coefficient distributions at five angles of attack for which simulations were performed for CC-1. It can be observed from the plots in Fig. 16 that the main element is the primary contributor to lift, as expected. While it is hard to discern from the C_p distributions, there is a small degree of flow separation on the aft upper surface of the main element for angles of attack higher than 13 deg. Flow remains attached to the lower surface for all angles of attack. Similar trends were observed for the rest of the four configurations of the closely-coupled multielement airfoil system.

C. Wake Bursting

Dynamics of wake interactions downstream of multielement airfoils can be highly complex and difficult to predict and compute. The pressure field off-the-surface of the multielement airfoil system is driven by the wake of the main element, the flap wake, and the wake of the jet through the gaps.[12] Interactions between the wakes shed from the different elements dominate the flowfield and can have a strong effect on the value of $C_{l_{max}}$.[11–13] In general, there is reduced aerodynamic performance of the multielement airfoil system if the wakes of the main and flap elements interact in any manner.[11]

Studies by Nakayama, et al.[12] show that the wake of the main element has the largest deficit in momentum and width. The low momentum wake of an upstream element can be adversely affected by the pressure gradients in the field of a downstream element. If the adverse pressure gradient is too great, the low momentum wake of the upstream element may experience an off-the-surface flow reversal. This separation is known as wake bursting. Wake bursting effectively decambers the airfoil system and leads to a loss in lift.[14,15] The region of the burst wake has a drop in static pressure, and the mean velocity in region approaches zero or negative values.[15,16] Experiments by Schneider, et al.[17] indicated the presence of two momentum deficit regions behind a multielement system when wake bursting occurred; one was the wake of the airfoil system and the other was the burst wake. Additional tests by Hoffenberg, et al.[18] suggested that the wakes in an adverse pressure gradient thicken, and the momentum deficit grows as the adverse pressure gradient strengthens.

Computational analysis was used to visualize off-the-surface flow downstream of the airfoil for the closely-coupled multielement airfoil configurations. Figure 17(a–e) shows the U/U_∞ contours for CC-1 for the computed angles of attack. Interaction between the wake of the main element and the boundary layer of the flaps can be observed in Fig. 17, as the angle of attack increases from 9 to 19 deg. With increase in flow turning angles, the adverse pressure gradient increases causing wake deceleration. The wake deceleration causes an

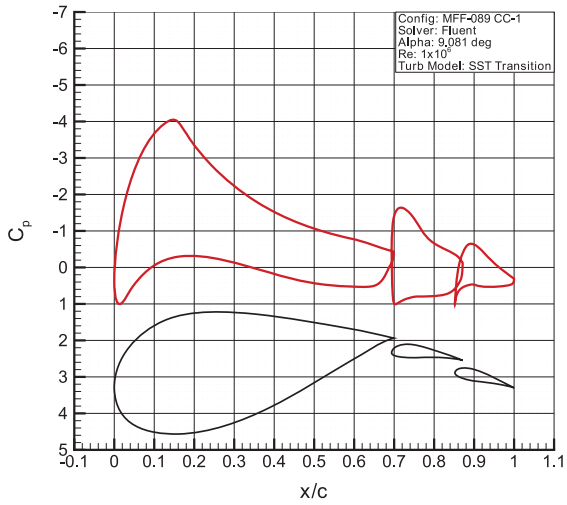

(a) $\alpha = 9.081$ deg

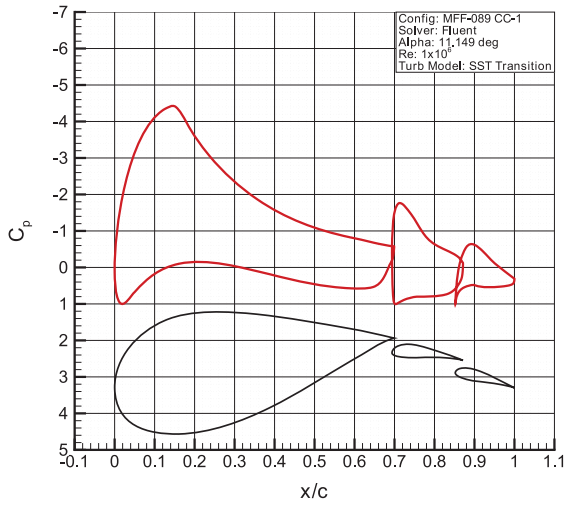

(b) $\alpha = 11.149$ deg

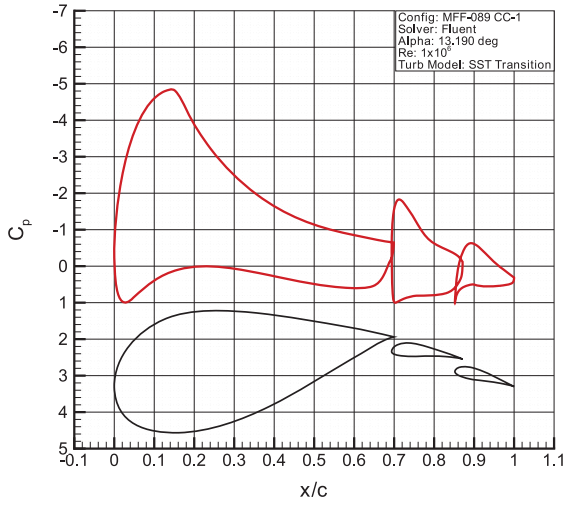

(c) $\alpha = 13.190$ deg

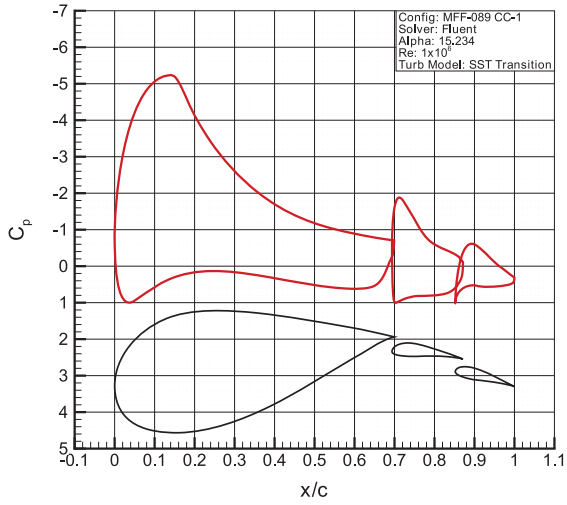

(d) $\alpha = 15.234$ deg

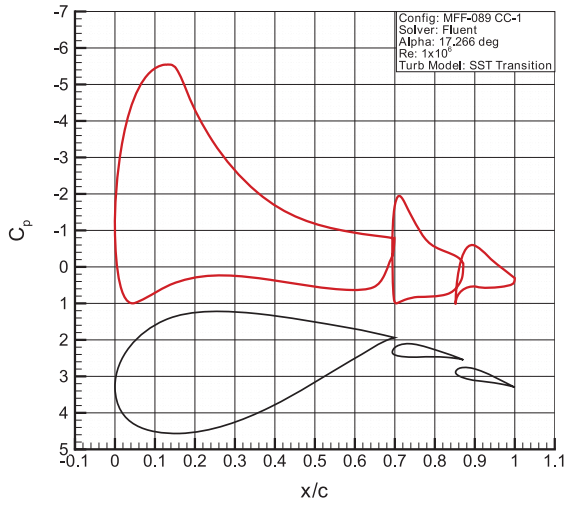

(e) $\alpha = 17.266$ deg

Figure 16. C_p **distributions for CC-1.**

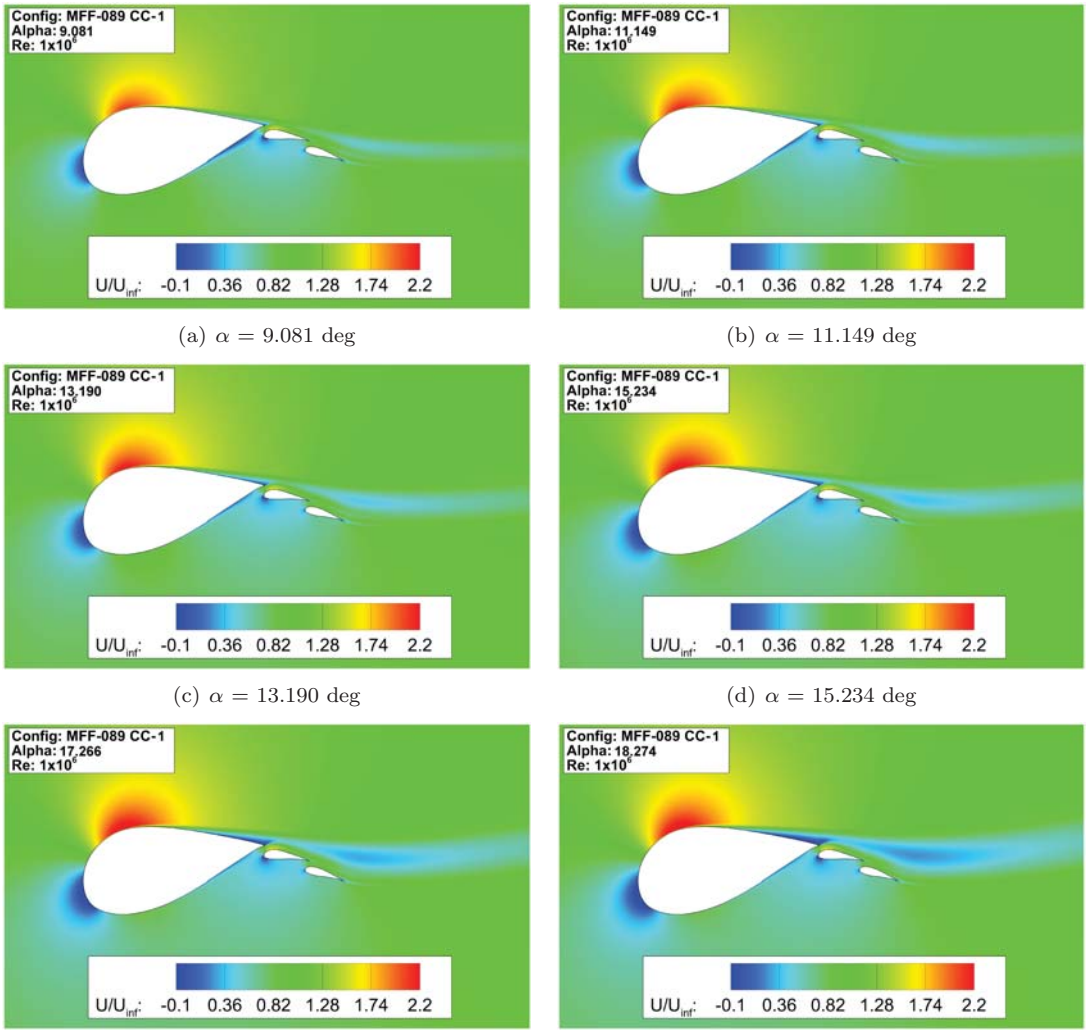

(a) $\alpha = 9.081$ deg

(b) $\alpha = 11.149$ deg

(c) $\alpha = 13.190$ deg

(d) $\alpha = 15.234$ deg

(e) $\alpha = 17.266$ deg

(f) $\alpha = 18.274$ deg

Figure 17. U/U_∞ **contours for CC-1.**

off-the-surface flow reversal (wake bursting) at higher angles of attack leading to an extra momentum deficit region behind the multielement system. In Fig. 17, the wake bursting is signified by the dark blue region above the flap elements at angles of attack above 13 deg.

Contour plots of U/U_∞ for the five closely-coupled configurations at the same angle of attack have been plotted in Figs. 18 and 19 to make a cross comparison of the wake bursting effects between configurations with constant gaps and overhangs and configurations with constant flap deflections.

Figure 18 shows the flow comparison between the configurations with constant gaps and overhangs and varying flap deflections. It can be observed from Fig. 18 that as the flap deflection increases, wake bursting increases. The increase in wake bursting can be attributed to the fact that with increasing flap deflections, the flow turning angles increase causing higher pressure gradients which physically translates to higher off-the surface flow reversal.

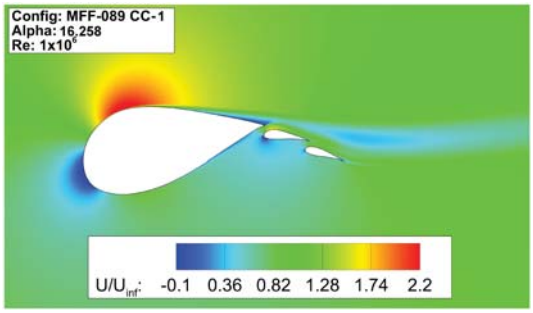

(a) U/U_∞ contour for CC-1 at $\alpha = 16.258$ deg

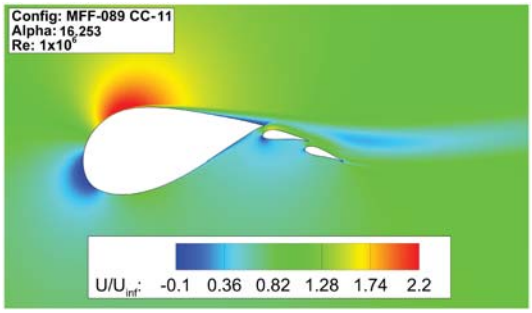

(b) U/U_∞ contour for CC-11 at $\alpha = 16.253$ deg

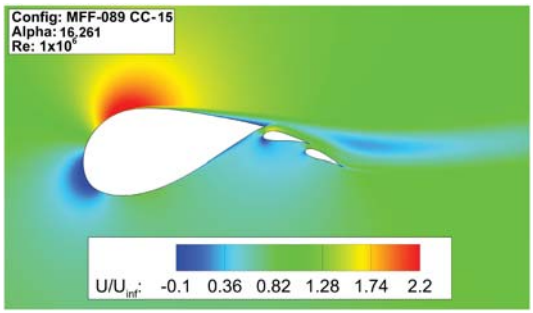

(c) U/U_∞ contour for CC-15 at $\alpha = 16.261$ deg

Figure 18. U/U_∞ contours comparison for varying flap deflection.

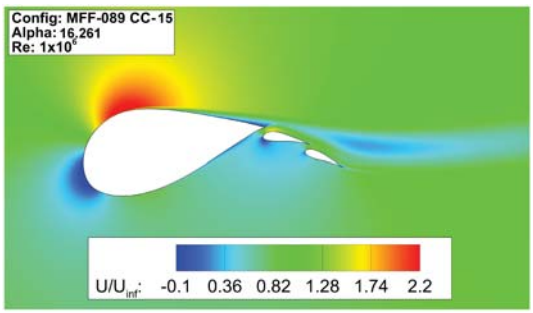

(a) U/U_∞ contour for CC-15 at $\alpha = 16.261$ deg

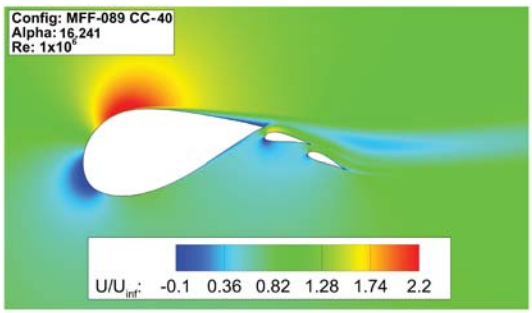

(b) U/U_∞ contour for CC-40 at $\alpha = 16.241$ deg

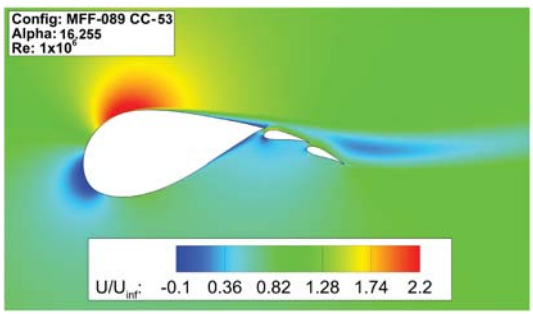

(c) U/U_∞ contour for CC-53 at $\alpha = 16.255$ deg

Figure 19. U/U_∞ contours comparison for varying gap and overhang.

Figure 19 shows the flow comparison between the configurations with constant flap deflections and varying gaps and overhangs. In the case of configuration CC-40, the gap is increased for both flaps while overhang is decreased as compared to CC-15. On the other hand, both gap and overhang are decreased for both flaps in configuration CC-53 as compared to CC-15. On comparing Fig. 19(a–b), it can be observed that an increase

in gap and decrease in overhang tends to decrease wake bursting. Increasing gap reduces the flow acceleration between the main and flap elements causing a decrease in the adverse pressure gradients. Figure 19(c) shows that decreasing the gap and overhang leads to higher wake bursting due to high pressure gradients caused by increased flow acceleration between the main element and flap. From Fig. 19, it can be concluded that reducing overhang has minimal effect on wake bursting of the closely-coupled multielement airfoil system. However, wake bursting is highly sensitive to the gap between the elements of the multielement airfoil system. Care must be taken to choose a proper gap size so as to have higher aerodynamic efficiency.

VI. Conclusions

Computational simulations were performed for five configurations of a closely-coupled multielement airfoil system consisting of a main element and two flap elements. The SST Transition turbulence model was used after the model was successfully validated against the experimental data of the NLR 7301 supercritical airfoil with flap. Following the turbulence model validation, grid validation studies were conducted using the baseline configuration of the closely-coupled multielement airfoil system, and grid parameters were fixed for all further computations. Simulations for each configuration were performed for nine angles of attack ranging between 9 to 20 deg.

On completion of the data analysis of the simulations of the closely-coupled multielement airfoil system, definite trends in C_l and C_d were observed across the closely-coupled configurations. The wake bursting phenomenon downstream of the airfoil was successfully captured by the computational model. Contour plots of U/U_∞ were studied to analyze the wake characteristics downstream of the airfoil. The C_l of the system was highly dependent on the flap deflection. Increase in flap deflection showed an increase in C_l. Minimal changes in C_d was observed for variation in flap deflection. Variations in flap gap and overhang had significant effects on the lift and drag data. Reduction in gap sizes and overhang distances had a negative effect on the aerodynamics of the airfoil due to an increase in wake bursting. The accelerated flow through the flap gaps resulted in higher off-the-surface flow reversal.

It is surmised that changes in flap gap, overhang, and deflection relative to the previous element can increase the aerodynamic efficiency of the multielement airfoil system. However, one best location of the flaps cannot be fixed due to the complex coupling of the effects due variation in flap gap, overhang, and deflection.

VII. Acknowledgments

Support for this research project was provided by GE Energy, National Science Foundation graduate research fellowship grant number 07-15088, and the UIUC Department of Aerospace Engineering.

References

[1]Wirz, R. E. and Johnson, P. M., "Aero-Structural Performance of Multiplane Wind Turbine Blades," AIAA Paper 2011-3025, Applied Aerodynamic Conference, Honolulu, HI, 2011.

[2]Ragheb, A. M. and Selig, M. S., "Multi-Element Airfoil Configurations for Wind Turbines," AIAA Paper 2011-3971, Applied Aerodynamics Conference, Honolulu, HI, 2011.

[3]Smith, A. M. O., "High-Lift Aerodynamics," *Journal of Aircraft*, Vol. 12, No. 6, June 1975, pp. 501–530.

[4]Langtry, R. and Menter, F., "Transition Modeling for General CFD Applications in Aeronautics," AIAA Paper 2005-0522, January 2005.

[5]Cebeci, T., Besnard, E., and Chen, H. H., "Calculation of Multielement Airfoil Flows, Including Flap Wells," AIAA Paper 96-0056, January 1996.

[6]van den Berg, B. and Oskam, B., "Boundary Layer Measurements on a Two-Dimensional Wing with Flap and a comparison with Calculations," AGARD CP-271, September 1979.

[7]Cerra, D. F. and Katz, J., "Design of a High-Lift Thick Airfoil for Unmanned Aerial Vehicle Applications," *Journal of Aircraft*, Vol. 45, No. 5, 2008, pp. 1789–1793.

[8]Ashby, D. L., "Experimental and Computational Investigation of Lift-Enhancing Tabs on a Multi-Element Airfoil," NASA TR 110432, NASA Ames Research Center, Moffet Field, CA, 1996.

[9]Celik, I., Ghia, U., Roache, P., and Freitas, C., "Procedure for Estimation and Reporting of Uncertainty Due to Discretization in CFD Applications," *Journal of Fluids Engineering*, Vol. 10, No. 7, July 2008, pp. 1–4.

[10]Biber, K. and Zumwalt, G. W., "Experimental Studies of a Two-Element Airfoil with Large Separation," AIAA Paper 92-0267, Aerospace Sciences Meeting, Reno, NV, 1992.

[11]Spaid, F. W., "High Reynolds Number Multielement Airfoil Flowfield Measurements," *Journal of Aircraft*, Vol. 37, No. 3, 2000, pp. 499–507.

[12]Nakayama, A., Kreplin, H., and Morgan, H., "Experimental Investigation of Flowfield About a Multielement Airfoil," *AIAA Journal*, Vol. 28, No. 12, 1988, pp. 14–21.

[13]Rogers, S. E., "Progress in High-Lift Aerodynamic Calculations," *Journal of Aircraft*, Vol. 31, No. 6, 1994, pp. 1244–1251.

[14]Hoffenberg, R. and Sullivan, J. P., "Simulation of High-Lift Wake Behavior," AIAA Paper 97-0718, Aerospace Sciences Meeting, Reno, NV, 1997.

[15]Driver, D. M. and Mateer, G. G., "Wake Flow in Adverse Pressure Gradient," *International Journal of Heat and Fluid Flow*, Vol. 223, 2002, pp. 564–571.

[16]Hoffenberg, R. and Sullivan, J. P., "Measurement and Simulation of Wake Deceleration," AIAA Paper 98-0522, Aerospace Sciences Meeting, Reno, NV, 1998.

[17]Schneider, S. P., Campbell, B., Bucci, G., and Sullivan, J. P., "An Experimental Simulation of Flap Flow on Multielement Airfoils at High Reynolds Number," AIAA Paper 94-2613, Aerospace Ground Testing Conference, Colorado Springs, CO, 1994.

[18]Hoffenberg, R., Sullivan, J. P., and Schneider, S. P., "Wake Measurements in a Strong Adverse Pressure Gradient," NASA CR 197272, 1995.